Hot deformation and processing maps of Al-15%B$_4$C composites containing Sc and Zr

Jian Qin, Zhan Zhang, X.-Grant Chen *

Department of Applied Science, University of Quebec at Chicoutimi, Saguenay (QC), Canada

G7H 2B1

Abstract

Hot deformation behavior and processing maps of three Al-15%B$_4$C composites denoted as the base composite (Al-15vol.%B$_4$C), S40 (Al-15vol.%B$_4$C-0.4wt.%Sc) and SZ40 (Al-15 vol.%B$_4$C-0.4wt.%Sc-0.24wt.%Zr) were studied by uniaxial compression tests performed at various deformation temperatures and strain rates. The constitutive equations of the three composites were established to describe the effect of the temperature and strain rate on hot deformation behavior. Using the established constitutive equations, the predicted flow stresses on various deformation conditions agreed well with the experimental data. The peak flow stress of the composites increased with the addition of Sc and Zr, attributing to the synthetic effect of solute atoms and dynamic precipitation. The addition of Sc and Zr increased the activation energy for hot deformation of Al-B$_4$C composites. The processing maps of the three composites were constructed to evaluate the hot workability of the composites. The safe domains with optimal deformation conditions were identified for all three composites. In the safe domains, dynamic recovery and

dynamic recrystallization were involved as softening mechanisms. The addition of Sc and Zr limited the dynamic softening process, especially for dynamic recrystallization. The microstructure analysis revealed that the flow instability was attributed to the void formation, cracking and flow localization during hot deformation of the composites.

Key words: Al-B$_4$C composites; Hot deformation; Processing map; Sc and Zr; Microstructure.

* Corresponding author:

Department of Applied Science, University of Quebec at Chicoutimi

Tel.: 1-418-545 5011 ext. 2603; Fax: 1-418-545 5012; E-mail: xgrant_chen@uqac.ca

1. Introduction

Aluminum-based metal matrix composites (MMCs) have gained popularity in industries due to their light weight, high strength and specific modulus, low coefficient of thermal expansion and good wear resistance compared to aluminum alloys [1]. The development of Al–B_4C composites has recently attracted increased attention, because they can serve as neutron absorbing material in transportation and storage of spent nuclear fuels in the nuclear industry, as boron carbide (B_4C) has a high cross-section for neutron absorption [2, 3]. The introduction of Sc and Zr into Al–B_4C composites can increase the composite strength at elevated temperatures by forming stable precipitates [4]. To manufacture a useful engineering product, most Al-based metal matrix composites are subjected to hot forming processes such as rolling, extrusion and forging. The mechanical properties of those composites are affected by their chemical composition and resultant microstructure from thermomechanical processing.

Several investigations found that dynamic precipitation (DPN) occurred during hot deformation in 2xxx, 6xxx and 7xxx series Al alloys [5-7]. The precipitation and subsequent coarsening can affect the flow curve and increase the flow stress level. The precipitates formed during hot deformation were reported to restrain dynamic recrystallization (DRX) and increase the activation energy for hot deformation [8]. It was reported that Sc and Zr could increase recrystallization resistance by forming $L1_2$ structure precipitates [9]. The fine precipitates of Al_3Sc could inhibit the migration of grain and sub-grain boundaries and the dislocation movement, thereby, restraining the recrystallization and resulting in a high work hardening stress [10, 11]. On

the other hand, the hot deformation behaviors of Al-based MMCs were also influenced by reinforcement particles, thermal residual stress, flow localization and deformation incompatibility between the matrix and enforcement particles [12, 13].

Constitutive equations are generally employed to predict the flow behavior of materials and to calculate their activation energies [14]. The activation energy for hot deformation Q is an important physical parameter that represents the difficulty level during hot deformation. The activation energy for hot deformation of pure Al was reported to be 144 kJ/mol [15]. The activation energy for an Al–5 wt.% B_4C composite was found to be 200.1 kJ/mol [16], which was higher than pure Al due to the presence of enforcement particles. In addition, the processing maps based on dynamic material models (DMM) have been widely employed to gain the optimum flow stability region and avoid the instability region [17]. Li *et al*. [18] studied the processing maps of a 6061 Al–B_4C composite in a wide range of temperatures and strain rates. Gangolu *et al*. [16] reported the hot workability of an Al-B_4C composite and proposed the optimum processing conditions in the form of a processing map.

The mechanical properties and microstructure evolution of Al–B_4C composites containing Sc and Zr have been studied in our previous works [19-21]. The present work focuses on the thermomechanical processing aspect of Al–B_4C composites containing Sc and Zr. The hot deformation behavior of three Al–B_4C composites, namely the base composite (Al-15vol.%B_4C), S40 (Al-15vol.%B_4C-0.4wt.%Sc) and SZ40 (Al-15vol.%B_4C-0.4wt.%Sc-0.24wt.%Zr), was investigated by hot compression tests performed at various temperatures and strain rates. The

constitutive equations and activation energies related to the peak flow stress, deformation temperature and strain rate were analyzed. The processing maps of three Al–B$_4$C composites were established to optimize the hot working processing. The deformation mechanisms were determined for both the flow stability and instability regions based on the microstructure observation using optical and scanning electron microscopes.

2. Experimental

Three Al-B$_4$C composites, namely the base composite, S40 and SZ40, were investigated in the present study. Their nominal chemical compositions are listed in Table 1. In the composite preparation process, commercially pure aluminum (99.7%) was first melted in a graphite-chamotte crucible in an electric resistance furnace. Master alloys Al-2 wt.% Sc, Al-15 wt.% Zr and Al-10 wt.% Ti were later added into the molten aluminum and the melt was held at 800 °C for 40 minutes to dissolve the master alloys. The prefabricated Al−25 vol.%B$_4$C with 2.0 wt.% Ti cast ingots, supplied by Rio Tinto Aluminum, was then placed in the alloyed melt. The average size of the B$_4$C particles (F360) was 23 μm. Under mechanical stirring using an impeller, the composite melts were held at 740 °C for 30 minutes and then cast into a rectangular permanent steel mold. The dimensions of the cast ingots were 30×40×80 mm.

Table 1. Nominal chemical compositions of experimental composites

Composite	Element				
	B$_4$C	Ti	Sc	Zr	Al
base composite	15 vol.%	1.5 wt.%	–	–	Bal.
S40	15 vol.%	1.5 wt.%	0.4 wt.%	–	Bal.
SZ40	15 vol.%	1.5 wt.%	0.4 wt.%	0.24 wt.%	Bal.

The cast ingots of S40 and SZ40 composites were heat-treated at 640 °C for 24 hours and 96 hours, respectively, followed by direct water quenching. The base composite was not heat-treated because of the non-heat-treatable nature of its 1100 matrix. The ingots were machined to cylindrical specimens, 10 mm in diameter and 15 mm in length, for compression tests. The compression tests were carried out using a Gleeble-3800 thermo-mechanical simulation unit at strain rates of 0.001, 0.01, 0.1 and 1 s^{-1} and deformation temperatures of 300, 350, 400, 450 and 500 ºC, respectively. During the compression tests, all specimens were heated to the desirable deformation temperature at a heating rate of 10 °C/s and held for 3 minutes to ensure the uniform temperature of the specimen. The specimens were deformed to a total true strain of 0.8.

For microstructure characterization, the deformed samples were cut parallel to the compression direction along the centerline. The samples were metallographically prepared and etched by a solution of 98 ml H$_2$O and 2 ml HF for 2 minutes for optical microstructure observation. Moreover, some deformed samples were analyzed using the electron back-scattered diffraction (EBSD) technique under a scanning electron microscope (SEM, JEOL JSM-6480LV).

3. Results and Discussion

3.1 Flow stress behavior

A series of typical true stress-strain curves of the base composite, S40 and SZ40 at various deformation temperatures and strain rates are presented in Fig. 1. Under all the test conditions, the flow stress had a rapidly increasing stage at the beginning of the deformation, which is due to the predominate effect of work hardening. In this stage, multiple dislocations and reactions among dislocations, defects and particles resulted in a large increase of dislocation migration resistance with increased the strain. With further increased strain, the increase rate of the flow stress gradually decreased, and the flow stresses either remained fairly constant or attained a maximum stress value before the flow stress decreased. During this stage, dynamic softening processes became operative and both dynamic softening and work hardening contribute more and less equally to the flow stress. However, at the low compression temperature of 300 ºC, the flow stress slowly but continuously increased after the rapid increasing stage (Fig. 1). In the present study, the peak stress is defined as the constant stress value for the case that the flow stresses remained constant after a rapidly increasing stage. For other cases, the maximum flow stress value in the flow curve is considered as the peak stress in the following discussion. Generally, the flow stress and peak stress of the three composites decreased with increasing deformation temperature and with decreasing strain rate. The same tendencies were observed in the previous research works on Al metal matrix composites [22, 23].

With the increase of deformation temperature, the bonding between atoms in the composite

7

matrix decreases, and the load transfer from the matrix to ceramic particles becomes weak [24], which directly weakens the flow stress. In addition, the high deformation temperature promotes atom diffusion and accelerated dislocation and grain boundary migrations, which results in a weaker work hardening and a stronger of dynamic softening. On the other hand, a low strain rate is favorable to the atom diffusion and dislocation migration, encouraging dynamic softening (DRX and DRV) [25]. Thus, on the effect of both high temperature and low strain rate, a lower flow stress and an earlier arrival of the steady state are reflected in the flow stress curves.
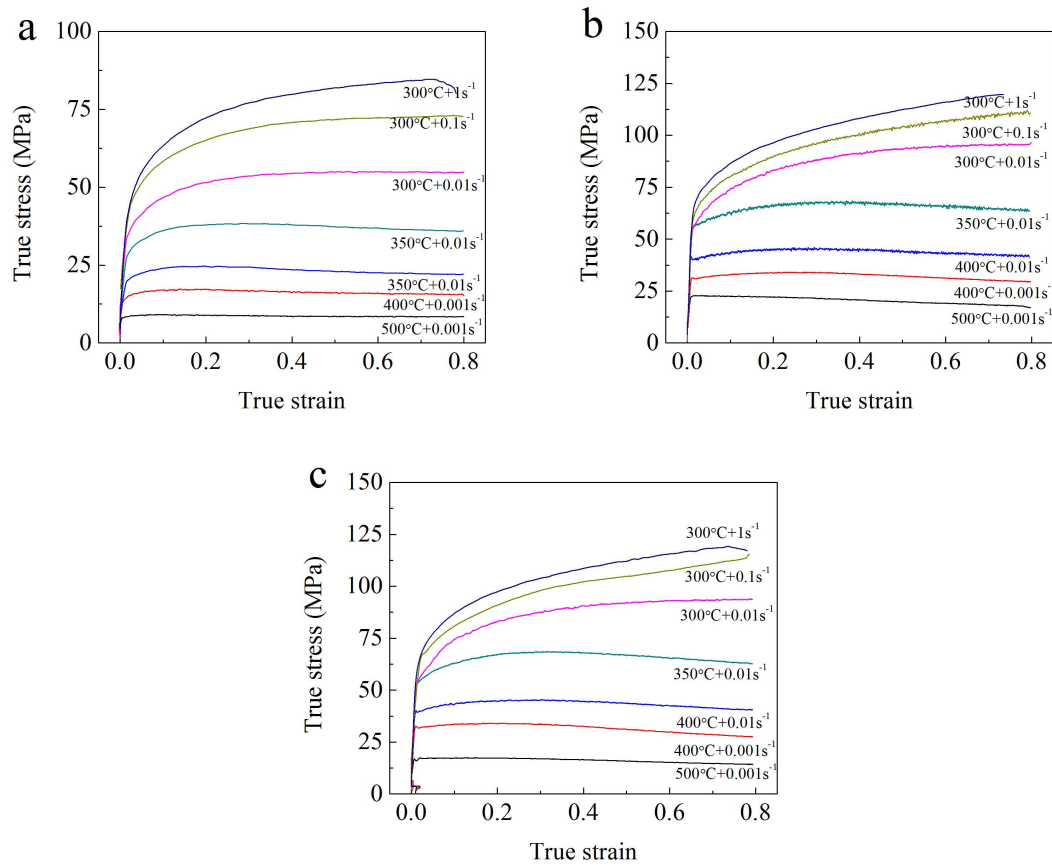

Fig. 1. Typical true stress–strain curves during hot compression deformation: (a) the base composite, (b) S40 and (c) SZ40 composites.

Fig. 2 illustrates the evolution of the peak stresses of the three composites at various deformation temperatures as a function of strain rate. In general, the peak stresses of the base material are obviously lower than that of S40 and SZ40 composites, while both peak stress values of S40 and SZ40 composites are close in all experimental conditions. For example, at 300 ºC and 0.001 s^{-1} strain rate, the peak stress of the base composite was 46 MPa, but the peak stresses of S40 and SZ40 were 76 MPa and 78 MPa, respectively. When the strain rate increased to 1 s^{-1} at the same temperature (300 ºC), the peak stress of the base composite was 82 MPa, but it reached 119 MPa for S40 and 120 MPa for SZ40. The same tendency of the peak stress evolution is observed in all deformation temperatures (Fig. 2). It is evident that the addition of Sc and Zr can remarkably enhance the deformation resistance during hot deformation at the temperatures from 300 to 500 ºC.

At a low deformation temperature (300 ºC), the peak stresses of S40 were slightly lower than that of SZ40, and the stress differences were approximately 1 to 6 MPa with various strain rates (Fig. 2a). However, at the high deformation temperature (500 ºC), the peak stresses of S40 were moderately higher than those of SZ40 (Fig. 2e). On the other hand, when the deformation temperatures were at 350-450 ºC, the difference of the peak flow stresses between S40 and SZ40 were almost negligible (Fig. 2b-d).

After the solution treatment of S40 and SZ40 samples before hot deformation, all Sc and Zr were dissolved in the composite matrix. At the deformation temperature below 400 ºC, there were no precipitates (Al$_3$Sc or Al$_3$(Sc,Zr)) found in the deformed microstructure of S40 and SZ40, which means that Sc and Zr solute atoms act as the barriers of dislocation movement at low

deformation temperatures. At high deformation temperatures (450-500 ºC), Al$_3$Sc and Al$_3$(Sc, Zr)

precipitates were observed in the deformed microstructure of S40 and SZ40 samples, indicating

that dynamic precipitation occurred during preheating and hot deformation. Similar phenomenon

was reported in other precipitation strengthening aluminum alloys [5, 6]. This results in the flow

stresses of S40 and SZ40 always being higher than that of the base composite at all deformation

conditions, because the addition of Sc and Zr hinder the dislocation migration either as solute

atoms at low temperatures or as precipitates at high temperatures.
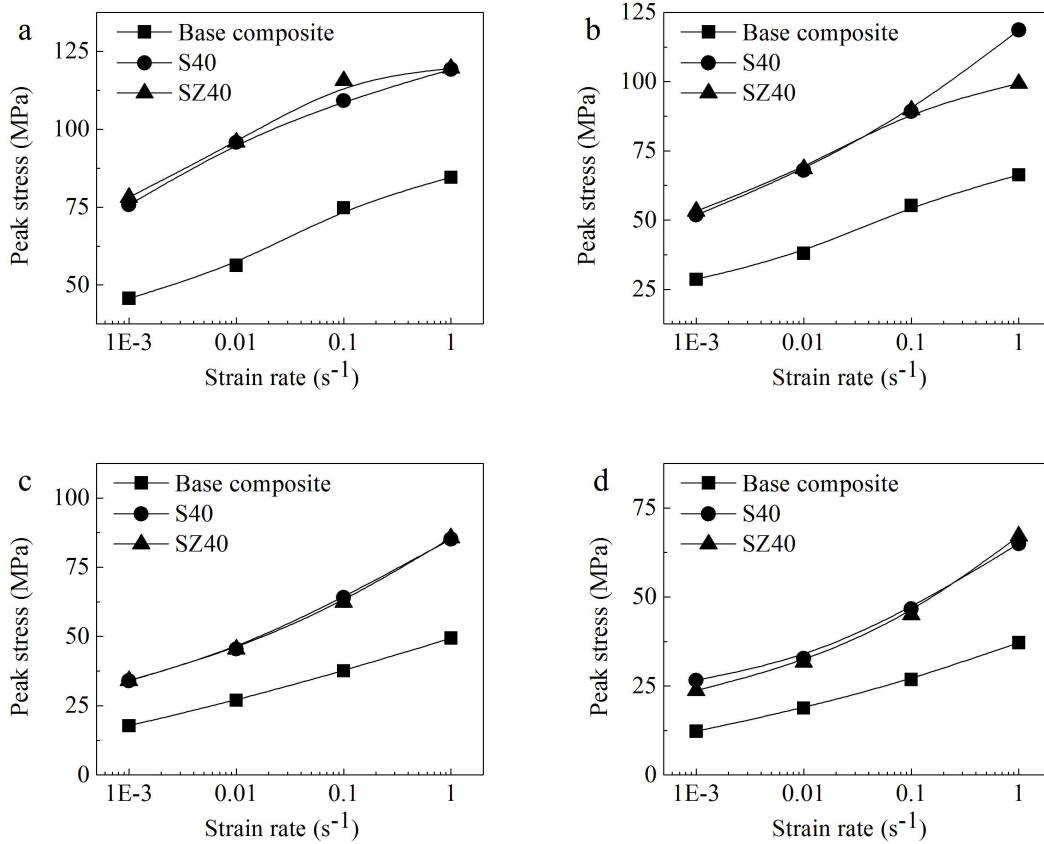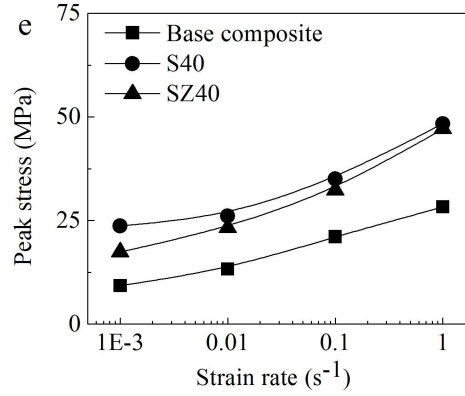
Fig. 2. Evolution of peak stresses of Al−B$_4$C composites at various temperatures as a function of strain rate: (a) 300 ºC, (b) 350 ºC, (c) 400 ºC, (d) 450 ºC and (e) 500 ºC.

3.2   Constitutive analyses

The hyperbolic-sine equation is usually applied to describes the relationship between strain rate, flow stress and deformation temperature for a large range of strain rate and stress levels [26]:

$$\dot{\varepsilon} = A\left[\sinh(\alpha\sigma)\right]^{n} \exp\left(-Q\Big/RT\right) \qquad \text{Eq. 1}$$

where, $\dot{\varepsilon}$ is the strain rate (s^{-1}); σ is the flow stress (MPa); T is the absolute temperature (K); R is the universal gas constant (8.314 J·mol^{-1}K^{-1}); and Q is the activation energy for hot deformation (kJ•mol^{-1}). In addition, A, n and α are material constants.

To obtain the materials constants and hot deformation activation energy, Eq. 2 is inducted by taking nature logarithm and differentiating Eq. 1:

$$Q = R\left[\frac{\partial\ln\dot{\varepsilon}}{\partial\ln\left[\sinh(\alpha\sigma)\right]}\right]_{T}\left[\frac{\partial\ln\left[\sinh(\alpha\sigma)\right]}{\partial(1/T)}\right]_{\dot{\varepsilon}} = RnS \qquad \text{Eq. 2}$$

The experimental data from the base composite, as an example, are shown in Fig. 3 to

11

demonstrate the derivation of materials constants and the calculation of activation energy for hot deformation. The peak stress σ_p is used here for σ, which represents the equilibrium condition between the work hardening and dynamic softening. Then, α can be deduced by the division result of β and n_1. The values of n_1 and β can be obtained from the mean slopes of the lines in the $\ln\dot{\varepsilon}$ vs. $\ln\sigma$ (Fig. 3a) and $\ln\dot{\varepsilon}$ vs. σ (Fig. 3b), respectively. Here, n is the mean slop of plots of $\ln\dot{\varepsilon}$ vs. $\ln\left[\sinh\left(\alpha\sigma\right)\right]$ at different temperatures (Fig. 3c). S is the mean slopes of $\ln\left[\sinh\left(\alpha\sigma\right)\right]$ vs. $1/T$ at various strain rates (Fig. 3d). Where the A can be obtained from the intercept of $\ln\left[\dot{\varepsilon}\exp\left(Q/RT\right)\right]$ vs. $\ln\left[\sinh\left(\alpha\sigma\right)\right]$ (Fig. 3e) [26].

Based on the above description and Eqs. 1 and 2, the calculated material constants A, n, α and the activity energy Q of the three composites are presented in Table 2. It is known that when the n is greater than 5, it indicates a climb-controlled dislocation deformation [27]. The n of three composites ranges from 5.17 to 6.70, which implies that the dislocation climb is the operative mechanism for three experimental composites during hot deformation. This agrees well with previous research [20].

The activation energy for hot deformation Q is an important physical parameter that represents the difficulty level in hot deformation. The activation energy of the base composite is calculated to be 186.4 kJ/mol (Table 2). With the addition of Sc and Zr (0.4% Sc in S40 and 0.4% Sc plus 0.24%Zr in SZ40), the values of the activation energy increase to 196.1 kJ/mol for S40 and 206.6 kJ/mol for SZ40, respectively, indicating that Sc and Zr in Al-B$_4$C composites considerably

increase the hot deformation resistance. This is most likely associated with the high solute level

and dynamic precipitation of Z40 and SZ40. At temperatures below 400 ºC, the Sc and Zr existed

as solute atoms in the composite matrix. Solute atoms can diffuse to dislocations acting as pins to

either restrict dislocation migration or drag a dislocation during slipping, which causes the

increase of the activation energy for hot deformation [5, 28]. On the other hand, Al_3Sc and $Al_3(Sc,$

Zr) nanoparticles dynamically precipitated at high temperatures (450-500 ºC) during hot

deformation. Those uniformly distributed precipitates acted as barriers of dislocation and subgrain

boundary migration, leading to the increase of the activation energy [5, 6, 29]. Compared to S40,

SZ40 has more solute atoms and more precipitates, resulting in a higher activation energy value

than S40. It is worth mentioning that the calculated activation energies in Table 2 are the average

values, because the activation energy for hot deformation is a function of deformation conditions

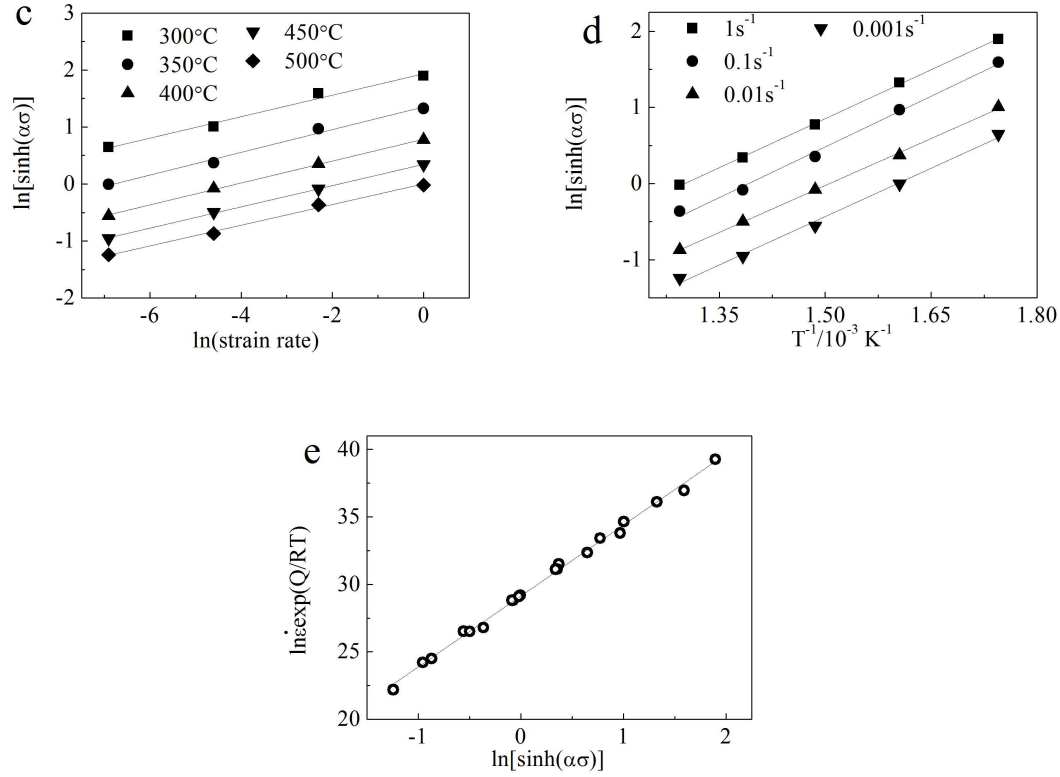(deformation temperature and strain rate) [14].
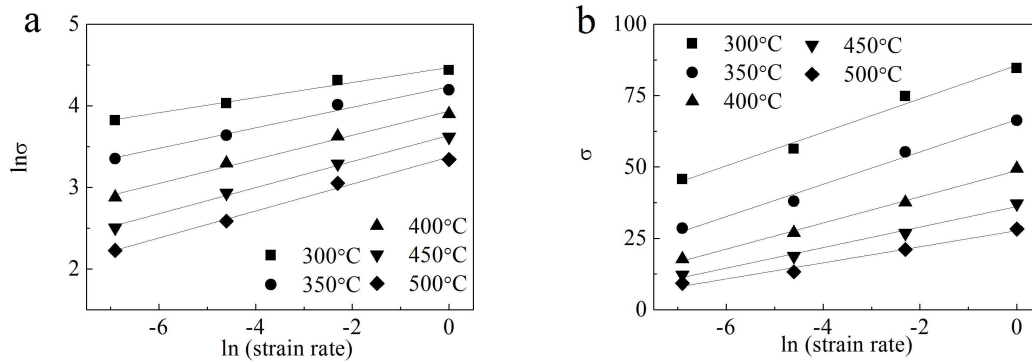
Fig. 3. Relationships between flow stress and strain rate for the base composite, (a) $\ln\sigma$ vs. $\ln\dot{\varepsilon}$, (b) σ vs. $\ln\dot{\varepsilon}$, (c) $\ln[\sinh(\alpha\sigma)]$ vs. $\ln\dot{\varepsilon}$, (d) $\ln[\sinh(\alpha\sigma)]$ vs. T^{-1} and (e) $\ln[\dot{\varepsilon}\exp(Q/RT)]$ vs. $\ln[\sinh(\alpha\sigma)]$.

Table 2. Values of the material constants and activation energy for the composites studied

Composites	α (MPa^{-1})	n	A (s^{-1})	Q (kj·mol^{-1})
Base	0.032	5.17	0.45×10^{13}	186.4
S40	0.017	6.70	1.30×10^{13}	196.1
SZ40	0.017	6.51	3.89×10^{13}	206.6

The effect of deformation temperature and strain rate on hot deformation behavior can be

expressed by Zener-Holloman parameter Z, as shown in Eq. 3 [30].

$$Z = \dot{\varepsilon}\exp\left(Q/RT\right) = A\left[\sinh\left(\alpha\sigma\right)\right]^{n} \qquad \text{Eq. 3}$$

Then, the flow stress σ can be described as a function of Z parameter based on the definition of

hyperbolic sine function:

$$\sigma = \frac{1}{\alpha}\ln\left\{\left(\frac{Z}{A}\right)^{1/n} + \sqrt{\left[\left(\frac{Z}{A}\right)^{2/n} + 1\right]}\right\}$$

Eq. 4

Hence, the relationship between flow stress, strain rate and deformation temperature of the

three composites can be expressed in Eqs. 5 to 7 based on Eq. 4 and the materials constants listed

in Table 2:

$$\sigma_{base} = 31.25\ln\left\{\left(\frac{\dot{\varepsilon}\exp\left(186.4/RT\right)}{0.45\times10^{13}}\right)^{0.19} + \sqrt{\left[\left(\frac{\dot{\varepsilon}\exp\left(186.4/RT\right)}{0.45\times10^{13}}\right)^{0.39} + 1\right]}\right\}$$

Eq. 5

$$\sigma_{S40} = 58.8\ln\left\{\left(\frac{\dot{\varepsilon}\exp\left(196.1/RT\right)}{1.3\times10^{13}}\right)^{0.15} + \sqrt{\left[\left(\frac{\dot{\varepsilon}\exp\left(196.1/RT\right)}{1.3\times10^{13}}\right)^{0.30} + 1\right]}\right\}$$

Eq. 6

$$\sigma_{SZ40} = 58.8\ln\left\{\left(\frac{\dot{\varepsilon}\exp\left(206.6/RT\right)}{3.89\times10^{13}}\right)^{0.15} + \sqrt{\left[\left(\frac{\dot{\varepsilon}\exp\left(206.6/RT\right)}{3.89\times10^{13}}\right)^{0.31} + 1\right]}\right\}$$

Eq. 7

Using the established constitutive equations (Eqs. 5−7), the predicted peak flow stresses vs.

the experimental data for the three composites are plotted in Fig. 4. The predicted peak stresses

show good agreement with the experimental peak stresses and the correlation coefficient is 99.6%,

97.3% and 98.3% for the base composite, S40 and SZ40, respectively, which indicate that the established constitutive equations (Eqs. 5−7) can give an accurate estimation of the peak stress values for all the three composites.
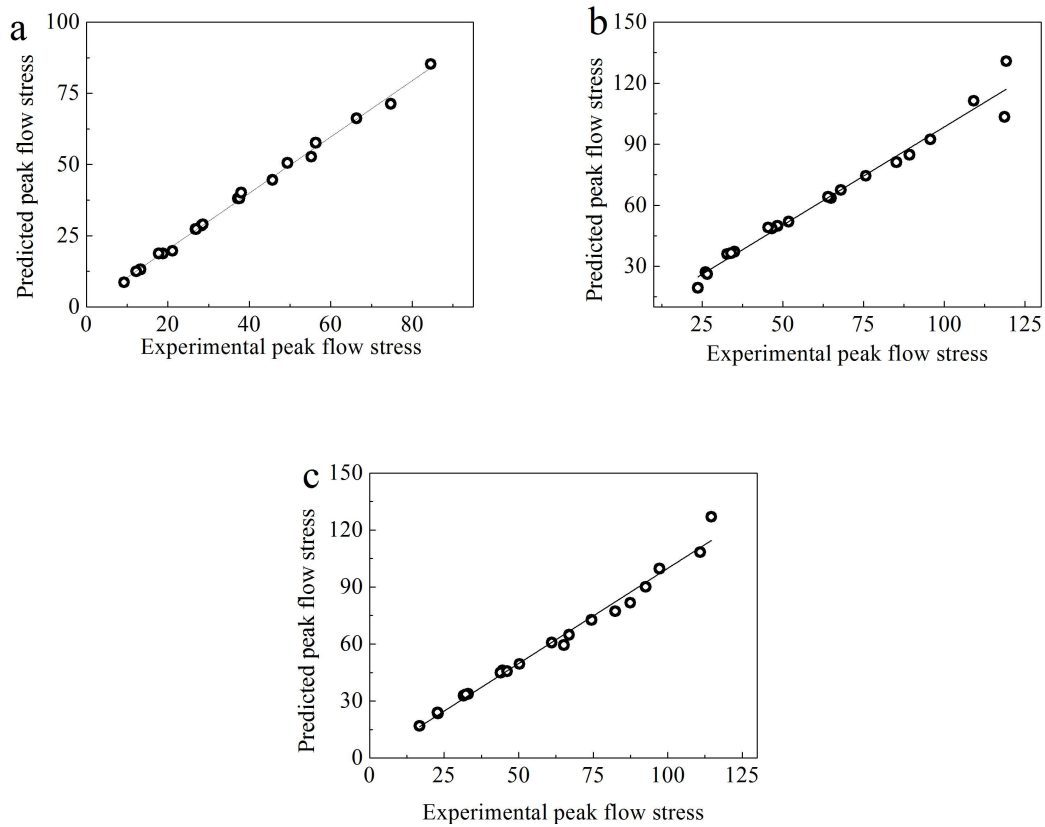

Fig. 4.　Predicted peak flow stress vs. experimental peak flow stress from the established constitutive equations: (a) the base composite, (b) S40 and (c) SZ40.

3.3 Processing maps

The hot workability on plastic deformation can be characterized based on the dynamic material model (DMM) [31]. In this model, the power dissipation is applied to describe the hot deformation behavior of materials. The efficiency of power dissipation η presents the energy

16

dissipated through the evolution of metallurgical mechanisms during the hot deformation, which is given in Eq. 8:

$$\eta = \frac{2m}{2m+1} \qquad \text{Eq. 8}$$

where m is the strain rate sensitivity of the materials determined by Eq. 9, which is varied with temperature and strain rate for composites [32]

$$m = \left(\frac{\partial \ln \sigma}{\partial \ln \dot{\varepsilon}} \right)_{T,\varepsilon} \qquad \text{Eq. 9}$$

In generally, the higher efficiency of power dissipation, the more power is considered to be dissipated by microstructure evolution, which implies a better hot workability. On the other hand, flow instability such as flow localization, shear bands and microcracks, etc. could occur under certain deformation conditions during the deformation. Flow instability could be predicted according to the continuum instability criterion shown as Eq.10 [33]:

$$\xi(\dot{\varepsilon}) = \frac{\partial \ln \left(\frac{m}{m+1} \right)}{\partial \ln \dot{\varepsilon}} + m \leq 0 \qquad \text{Eq. 10}$$

Therefore, the deformation parameters have to select the cases where the ξ is larger than zero during the plastic deformation.

To describe the relationship between hot workability and flow instability, the contour plots of the iso-efficiency of power dissipation η and the iso-flow instability ξ as a function of temperature and strain rate can be plotted together to construct the processing map. Fig. 5 shows the processing maps developed for the three composites at the true strain of 0.8. The values of the power dissipation efficiency η are shown as contour numbers, while the shaded area denotes the instability region. A safe domain should have higher dissipation efficiency and avoid the instability

17

region in the process map. The recommended safe domains based on power dissipation efficiency and flow instability are shown in Fig. 5 and the corresponding values are listed Table 3. For the base composite, the processing map exhibits three safe domains (Fig. 5a). Domain I with the power dissipation efficiency of 0.27-0.30 is located at the temperatures of 475-500 °C and the strain rates of 0.1-1 s^{-1}. Domain II with the power dissipation efficiency of 0.27-0.28 is on the region with lower temperatures and lower strain rates (330-400 °C/0.007-0.001 s^{-1}), while Domain III has the same power dissipation efficiency as Domain II but its working region is at higher temperatures (420-470 °C). For S40, there are two safe domains (Fig. 5b): one with the power dissipation efficiency of 0.26-0.28 at the zone having high temperatures (400-500 ºC) and high strain rates (0.11-1 s^{-1}) and another one with the efficiency of 0.26 with low temperatures (340-380 ºC) and low strain rates (0.01-0.001 s^{-1}). The two safe domains in SZ40 are similar to those in S40 (Fig. 5c). Compared three processing maps in Fig. 5, the domains I of S40 and SZ40 are situated at the similar region as the domain I of the base composite, but they expand toward lower temperate with lower efficiency. The processing ranges of the domains II of S40 and SZ40 are also similar to the domain II of the base composite. However, the base composite possesses another additional safe domain (III) at low strain rates, indicating a better hot workability than S40 and SZ40 composites.

The flow instability region of the base composite covers from 300 to 350 °C at high strain rates of 0.04 to 1 s^{-1} (Fig. 5a). With the addition of Sc, the flow instability region of S40 expands toward lower strain rates, which is situated from 300 to 350 °C at low strain rates of 0.002 to 1 s^{-1}

18

(Fig. 5b). Moreover, with the addition of Sc and Zr, the flow instability region of SZ40 becomes

even larger than that of S40 and it extends up to the temperature of 380 °C (Fig. 5c). This indicates

that the addition of Sr and Zr remarkably decreases the processing window of hot deformation. It is

evident that the flow instability regions in all three composites present lower values of power

dissipation efficiencies, compared with the adjacent stable regions. Therefore, the processing

parameters should not be chosen in the instability regions of those composites to obtain good hot

workability and to prevent the occurrence of deformation defects.

Table 3. Safe processing domains of three composites

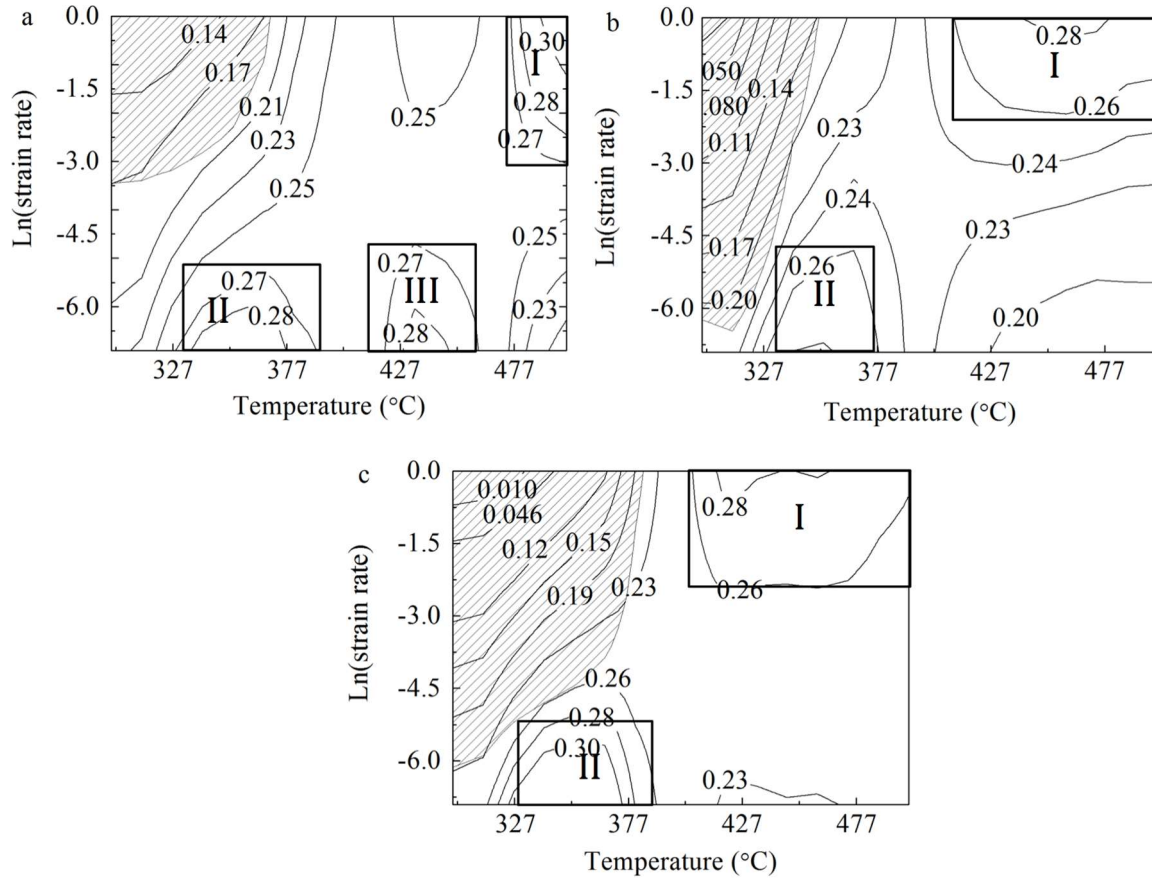| Composites	High strain rate domains (I)		Low strain rate domains (II & III)	
Base	475−500 °C	0.05−1 s^{-1}	330−400 °C	0.007−0.001 s^{-1}
			420−470 °C	0.008−0.001 s^{-1}
S40	400−500 °C	0.11−1 s^{-1}	340−380 °C	0.010−0.001 s^{-1}
SZ40	400−500 °C	0.11−1 s^{-1}	327−390 °C	0.007−0.001 s^{-1}

Fig. 5. Processing maps of three composites developed at the true strain of 0.8: (a) the base composite, (b) S40 and (c) SZ40.

3.4 Microstructure evolution

3.4.1 Deformed microstructure at various deformation conditions

Fig. 6 shows the optical microimages of three composites deformed at 300 °C and 1 s^{-1}. The original as-cast equiaxed grains [26] were greatly elongated and severe deformation bands (the arrows in Fig. 6) were present. Those deformation bands did not distribute uniformly and more

deformation bands concentrated near B_4C particles, which indicated that B_4C particles cause the local stress concentration. EBSD orientation maps were used to understand the dynamic softening mechanisms during hot deformation. The orientation maps of the base composite and SZ40, as examples, are shown in Fig. 7. A large amount of dislocation cells and subgrains with low-angle boundaries of 1-15º appeared in the base and SZ40 composites, which are typically recovered microstructure. There was a small amount of recrystallized grains with a small size of 1-3μm along the grain boundaries in the matrix of the base composite (Fig. 7a). In SZ40, the recrystallized grains were hardly found in the matrix. In overall, the predominant softening mechanism is dynamic recovery for the three composites deformed at the low temperature of 300 ºC.
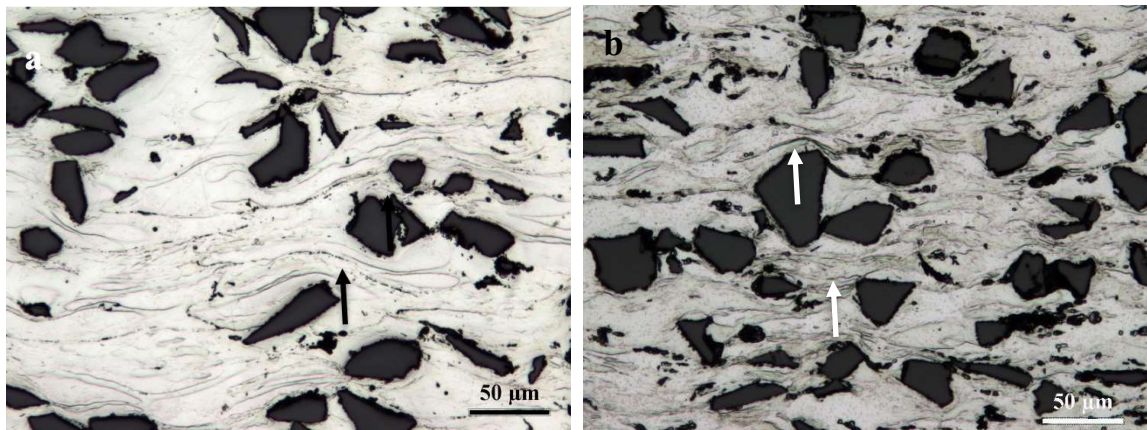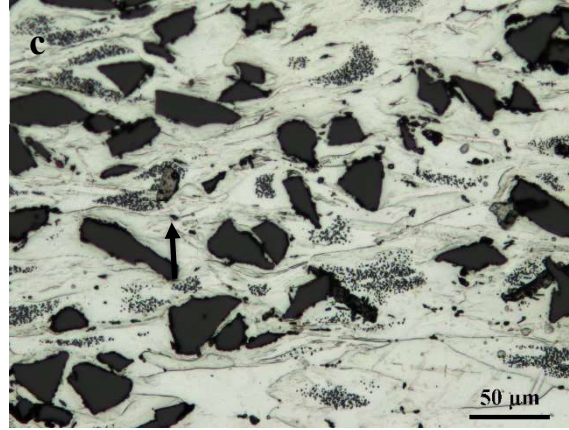
Fig. 6. Optical microstructures deformed at 300 ºC and 1 s^{-1} with a true strain of 0.8: (a) base composite, (b) S40 and (c) SZ40 composites.
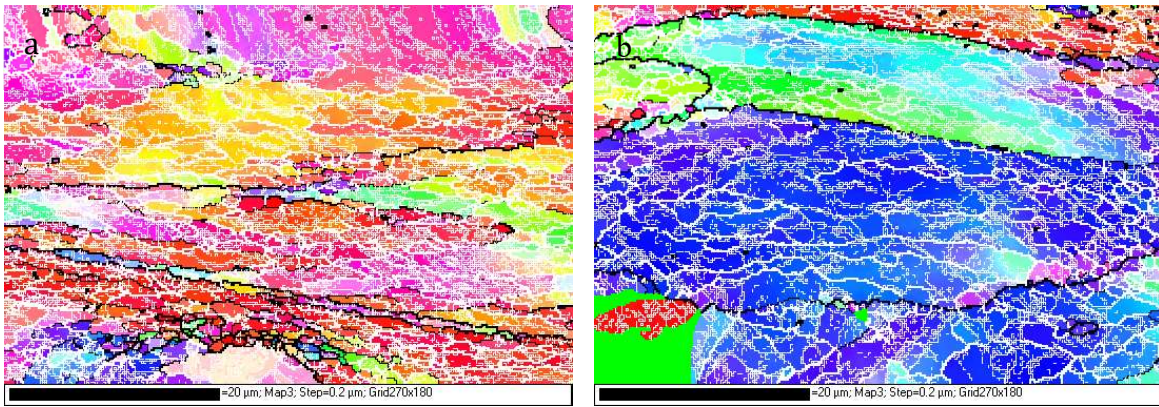

Fig. 7. EBSD orientation maps deformed at 300 ºC and 1 s^{-1}: (a) the base composite and (b) SZ40 composite. Boundary misorientation as indicated: thin white lines: 1~5°; thick white lines: 5~15°; black lines: >15°.

When deformed at higher temperature (500 ºC and 1 s^{-1}), a number of recrystallized grains with a size range of 5-50 μm appeared in the base composite (arrows in Fig. 8a), while only a few recrystallized grains with a small size of 1-3 μm presented in S40 and SZ40 samples (Fig. 8b).

EBSD orientation maps confirmed that the deformed microstructure in S40 and SZ40 were primarily recovered structure (Fig. 9), indicating that the addition of Sc and Zr impedes the recrystallization in the Al-B$_4$C composites. When deformed at 500 ºC with a lower strain rate of 0.001 s^{-1}, the microstructure of the base composite remained the recrystallized structure but the recrystallized grains became larger than those deformed at 500 ºC and 1 s^{-1}. For S40 and SZ40, the deformed microstructures remained as dynamically recovered structure but a small amount of fine recrystallized grains inhomogeneously distributed along the deformation bands. Therefore, it can be concluded that, at the high temperature of 500 ºC, dynamic recrystallization (DRX) is the main softening mechanism for the base composite deformation, while the predominant softening mechanism was dynamic recovery (DRV) for S40 and SZ40.

Dynamic softening processes, including dynamic recovery and dynamic recrystallization, involves rearrangement and annihilation of dislocations, and subgrain generation and migration. When the hot deformation at lower temperatures, for example 300 ºC, Sc and Zr atoms, dissolved in the matrix after solution treatment, could segregate around dislocations and into subgrain boundaries to lower the system energy, which results in the increase of the resistance of dislocation and subgrain migration during the deformation. Moreover, as the deformation at high temperatures, for example 500 ºC, occurs, the dynamically precipitated Al$_3$Sc and Al$_3$(Sc, Zr) nanoparticles have a strong pinning effect on dislocation and subgrain migrations [5, 6, 29]. Therefore, the additions of Sc and Zr can remarkably limit the dynamic softening process, especially for dynamic recrystallization.
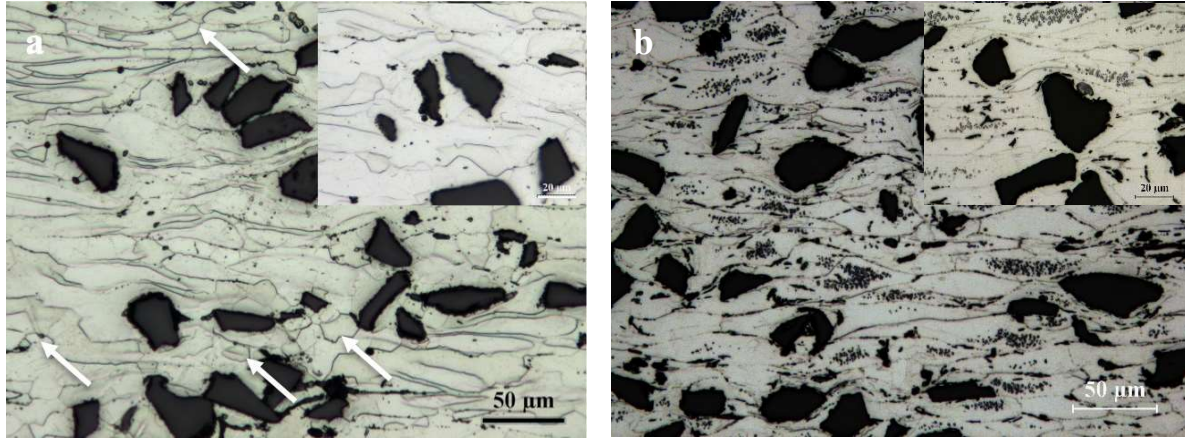
Fig. 8. Optical microstructures deformed at 500 ºC and 1 s^{-1} with a true strain of 0.8: (a) the base composite and (b) SZ40 composite.
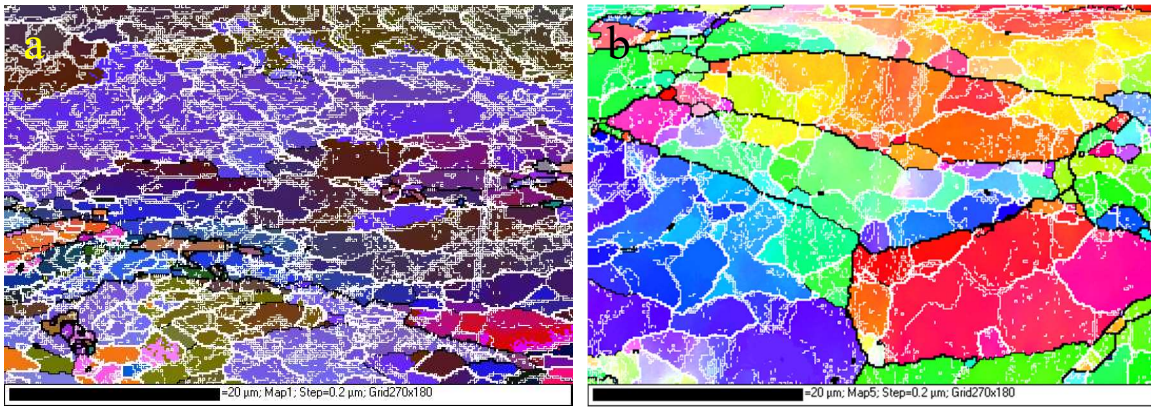

Fig. 9. EBSD orientation maps deformed at 500 ºC and 1 s^{-1} with a true strain of 0.8: (a) S40 and (b) SZ40 composites.

3.4.2 Microstructure features in flow stability and instability domains

The safe domains I in the processing maps of the three composites (Fig. 5) are all located in the region with high temperature (400-500 ºC) and high strain rate (0.1-1 s^{-1}). The microstructures of three composites in the domain I are identical as those shown in Figs. 8 and 9. It is evident that

in the domain I, DRX was the main softening mechanism for the base composite and DRV was the predominant softening mechanism for S40 and SZ40.

The typical microstructures in the safe domains II of three composites are shown in Fig. 10. Deformed at 350ºC and 0.001 s^{-1} (Fig. 10a), the microstructure of the base composite consisted of a large amount of dislocation cells and subgrains with low-angle boundaries of 1-15° and a few of recrystallized grains, which indicated that DRV mainly controls the softening process. The microstructure of the base composite in the domain III is similar to that in the domain II, but the size of recrystallized grains is slightly larger than that in domain II. The deformed microstructures of S40 and SZ40 in domain II were primarily recovered structure. For example, the microstructure of SZ 40 deformed at 350ºC and 0.001 s^{-1} exhibited mainly elongated grains with a number of cells and subgrains (Fig. 10b). Hence, the main softening mechanism in the safe domains II and III of the base material as well as the safe domains II of S40 and SZ40 composites was DRV.
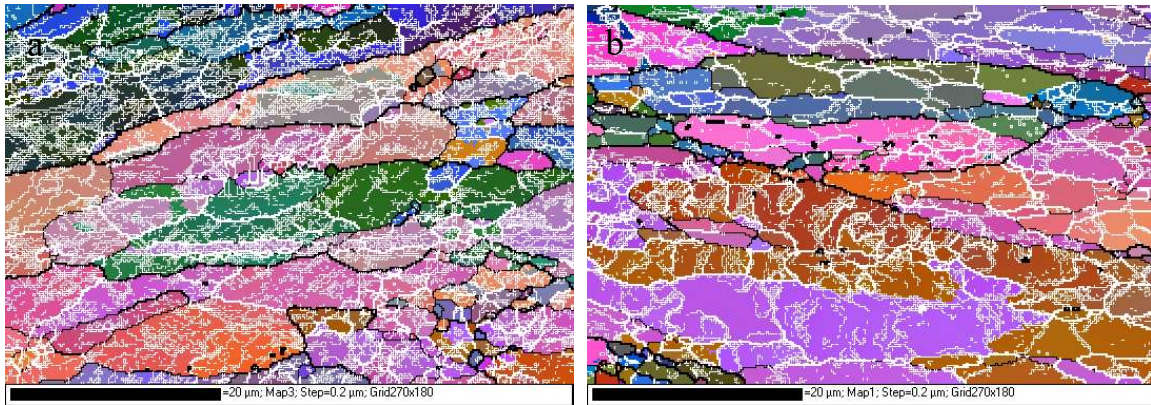

Fig. 10. Typical EBSD orientation maps in the safe domain II under the deformation condition at 350 ºC and 0.001 s^{-1}: (a) the bas composite and (b) SZ40.

The flow instability region of the base composite is located at low temperatures (300-350 ºC) with high strain rates of 0.04-1 s^{-1} and the instability regions of S40 and SZ40 extend toward the higher temperatures of up to 380 ºC and the lower strain rates of up to 0.002 s^{-1} (Fig. 5). Deformation defects, such as voids and cracks, were observed in the flow instability regions of deformed samples. Fig. 11 shows some examples of deformed microstructures with the deformation condition at 300 ºC and 1 s^{-1} for the base composite and SZ40 (Fig. 11a and c) and for S40 at 300 ºC and 0.01 s^{-1} (Fig. 11b), located in the flow instability regions. Except for the deformation bands and elongated grains in the matrix, the deformation defects such as voids, cracks and flow localization were often observed around B$_4$C particles (arrows in Figs. 11a, b and c). It is suggested that the defect formation is the major cause for the flow instability during hot deformation of Al-B$_4$C composites.
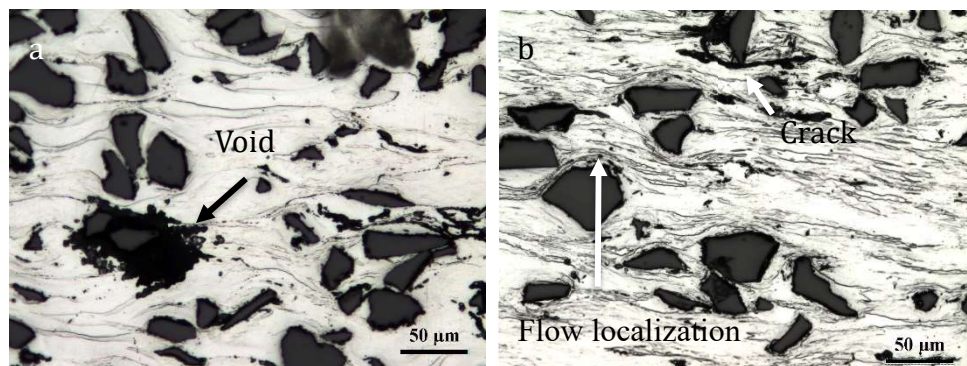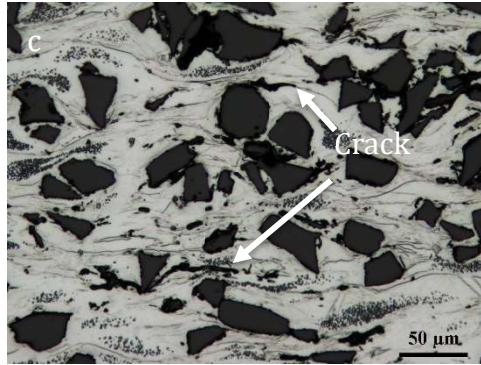
Fig. 11. Microstructures of (a) the base composite deformed at 300 ºC and 1 s^{-1}, (b) S40 deformed at 300 ºC and 0.01 s^{-1} and (c) SZ40 deformed at 300 ºC and 1 s^{-1}.

4.   Conclusions

1) The flow stress increased with the increase of the strain rate and the decrease of the deformation temperature during hot deformation. The addition of Sc and Zr in Al-15%B$_4$C composites increased the flow stress, which was attributed to the synthetic effect of solute atoms and dynamic precipitation.

2) With the addition of Sc and Zr, the activation energy for hot deformation increased from 186.4 kJ/mol for the base composite to 196.1 kJ/mol for S40 composite containing 0.4% Sc, and further to 206.6 kJ/mol for SZ40 composite containing 0.4% Sc and 0.24%Zr.

3) The predominant softening mechanism was dynamic recovery for three composites at the low deformation temperature (300 ºC). When the deformation temperature increased to 500 ºC, dynamic recrystallization became the main softening mechanism for the base composite, while dynamic recovery still controlled the softening process for S40 and SZ40.

4) Constitutive equations of three composites were established based on the hyperbolic-sine

27

equation and the experimental compression data. The predicted peak flow stresses on various deformation conditions were in good agreement with the experimental data for all the three composites.

5) The processing maps of three composites were constructed at the 0.8 strain based on the dynamic materials model. The safe domains with optimal deformation conditions were identified and the hot workabilities of the three composites were compared.

6) The flow instability region of the base composite was located at low deformation temperatures (300-350 ºC) and high strain rates (0.04 to $1s^{-1}$). The addition of Sc and Zr extended the instability regions toward the higher temperatures of up to 380 ºC and the lower strain rates of up to 0.002 s^{-1} for S40 and SZ40 composites. The defects generated during hot deformation, such as voids, cracking and flow localization around B_4C particles, were the major cause for the flow instability.

References

1. I.A. Ibrahim, F.A. Mohamed, and E.J. Lavernia, Particulate reinforced metal matrix composites − a review, *J. Mater. Sci.*, 1991, **26**(5), p 1137-1156

2. J.X. Deng and J.L. Sun, Microstructure and mechanical properties of hot-pressed $B_4C/TiC/Mo$ ceramic composites, *Ceram. Int.*, 2009, **35**(2), p 771-778

3. T.K. Roy, C. Subramanian, and A.K. Suri, Pressureless sintering of boron carbide, *Ceram. Int.*, 2006, **32**(3), p 227-233

4. C.B. Fuller, D.N. Seidman, and D.C. Dunand, Mechanical properties of Al(Sc,Zr) alloys at ambient and elevated temperatures, *Acta Mater.*, 2003, **51**(16), p 4803-4814

5. X. Huang, H. Zhang, Y. Han, W. Wu, and J. Chen, Hot deformation behavior of 2026 aluminum alloy during compression at elevated temperature, *Mater. Sci. Eng. A*, 2010, **527**(3), p 485-490

6. H. Zhang, L. Li, D. Yuan, and D. Peng, Hot deformation behavior of the new Al-Mg-Si-Cu aluminum alloy during compression at elevated temperatures, *Mater. Charact.*, 2007, **58**(2), p 168-173

7. E. Cerri, E. Evangelista, A. Forcellese, and H. McQueen, Comparative hot workability of 7012 and 7075 alloys after different pretreatments, *Mater. Sci. Eng., A*, 1995, **197**(2), p 181-198

8. Y. Li, Z. Liu, L. Lin, J. Peng, and A. Ning, Deformation behavior of an Al-Cu-Mg-Mn-Zr alloy during hot compression, *J. Mater. Sci.*, 2011, **46**(11), p 3708-3715

9. M.E. Drits, L.S. Toropova, Y.G. Bykov, F.L. Gushchina, V.I. Elagin, and Y.A. Filatov, Metastable state diagram of the Al-Sc system in the range rich in aluminum, *Russ. Metall.*, 1983, (1), 150-153

10. T.G. Nieh, L.M. Hsiung, J. Wadsworth, and R. Kaibyshev, High strain rate superplasticity in a continuously recrystallized Al-6%Mg-0.3%Sc alloy, *Acta Mater.*, 1998, **46**(8), 2789-2800

11. C.B. Fuller, A.R. Krause, D.C. Dunand, and D.N. Seidman, Microstructure and mechanical properties of a 5754 aluminum alloy modified by Sc and Zr additions, *Mater. Sci. Eng. A*, 2002, **338**(1-2), p 8-16

12. I. Dutta, J. Sims, and D. Seigenthaler, An analytical study of residual stress effects on uniaxial

deformation of whisker reinforced metal-matrix composites, *Acta Metall. Mater.*, 1993, **41**(3), p 885-908

13. C. Chen, S. Qin, S. Li, J. Wen, Finite element analysis about effects of particle morphology on mechanical response of composites, *Mater. Sci. Eng. A*, 2000, **278**(1), 96-105

14. C.J. Shi, W.M. Mao, and X.G. Chen, Evolution of activation energy during hot deformation of AA7150 aluminum alloy, *Mater. Sci. Eng. A*, 2013, **571**, p 83-91

15. W.F. Gale and T.C. Totemeier, *Smithells metals reference book*, Butterworth-Heinemann, Oxford, 2003

16. S. Gangolu, A. Rao, N. Prabhu, V. Deshmukh, and B. Kashyap, Hot workability and flow characteristics of aluminum-5 wt.% B4C composite, *J. Mater. Eng. Perform.*, 2014, **23**(4), p 1366-1373

17. Y.V.R.K. Prasad, K.P. Rao, and S. Sasidhara, *Hot working guide: a compendium of processing maps*, ASM international, Ohio, 1997

18. H. Li, H. Wang, M. Zeng, X. Liang, and H. Liu, Forming behavior and workability of 6061/B$_4$CP composite during hot deformation, *Compos. Sci. Technol.*, 2011, **71**(6), p 925-930

19. J. Qin, Z. Zhang, and X. Chen, Effect of hot deformation on microstructure and mechanical properties of Al-B$_4$C composite containing Sc, *Mater. Sci. Forum*, 2014, **794-796**, p 821-826

20. J. Qin, Z. Zhang, and X. Chen, Mechanical Properties and Strengthening Mechanisms of Al-15 Pct B$_4$C Composites with Sc and Zr at Elevated Temperatures, *Metall. Mater. Trans. A*, 2016, **47**(9), p 4694-4708

21. J. QIN, Z. Zhang, and X-Grant CHEN, Mechanical properties and thermal stability of hot-rolled Al–15%B4C composite sheets containing Sc and Zr at elevated temperature, *J. Comp. Mater.*, 2016, online published, DOI: 10.1177/0021998316674351

22. T. Srivatsan and J. Mattingly, Influence of heat treatment on the tensile properties and fracture behaviour of an aluminium alloy-ceramic particle composite, *J. Mater. Sci.*, 1993, **28**(3), p 611-620

23. T. Christman, A. Needleman, and S. Suresh, An experimental and numerical study of deformation in metal-ceramic composites, *Acta Metall.*, 1989, **37**(11), p 3029-3050

24. Z. Ma and S. Tjong, Creep deformation characteristics of discontinuously reinforced aluminium-matrix composites, *Compos. Sci. Technol.*, 2001, **61**(5), p 771-786

25. X. Wang, K. Wu, W. Huang, H. Zhang, M. Zheng, and D. Peng, Study on fracture behavior of particulate reinforced magnesium matrix composite using in situ SEM, *Compos. Sci. Technol.*, 2007, **67**(11), p 2253-2260

26. C. Sellars and W.M.G. Tegart, Relation between flow stress and structure in hot deformation, *Mem. Etud. Sci. Rev. Met.*, 1966, **67**(9), p 731-746

27. H. Lüthy, R.A. White, and O.D. Sherby, Grain boundary sliding and deformation mechanism maps, *Mater. Sci. Eng.*, 1979, **39**(2), p 211-216

28. H.J. McQueen, S. Spigarelli, M.E. Kassner, and E. Evangelista, *Hot deformation and processing of aluminum alloys*, CRC Press, New York, 2011

29. P. Wouters, B. Verlinden, H. McQueen, E. Aernoudt, L. Delaey, and S. Cauwenberg, Effect of homogenization and precipitation treatments on the hot workability of an aluminium alloy AA2024, *Mater. Sci. Eng. A*, 1990, **123**(2), p 239-245

30. H.R. Ashtiani, M. Parsa, and H. Bisadi, Constitutive equations for elevated temperature flow behavior of commercial purity aluminum, *Mater. Sci. Eng. A*, 2012, **545**, p 61-67

31. Y. Prasad, H. Gegel, S. Doraivelu, J. Malas, J. Morgan, K. Lark, and D. Barker, Modeling of dynamic material behavior in hot deformation: forging of Ti-6242, *Metall. Trans., A*, 1984, **15**(10), p 1883-1892

32. P. Dadras and J. Thomas, Characterization and modeling for forging deformation of Ti-6Ai-2Sn-4Zr-2Mo-0.1 Si, *Metall. Trans., A*, 1981, **12**(11), p 1867-1876

33. A.K. Kumar, *Criteria for predicting metallurgical instabilities in processing maps*, Indian Institute of Science, Bangalore, 1987